Research
A SCIENCE PARTNER JOURNAL

RESEARCH ARTICLE

Covalently Tethering Atomically Precise Au_{25} Nanoclusters onto Covalent Organic Framework for Visible-Light-Driven CO_2 Reduction

Ping Fu[1], Biao Meng[1,2,3], Qizhi Hu[1], Jiao Wei[1], Qihong Yue[1], Mingdong Sun[1], Qing Xu[1], Xiaoling Liu[1], Shibo Xi[4], Wen Yin[2,3], Yu Zhou[1*], and Jun Wang[1*]

[1]State Key Laboratory of Materials-Oriented Chemical Engineering, College of Chemical Engineering, Nanjing Tech University, Nanjing 211816, China. [2]University of Chinese Academy of Sciences, Chinese Academy of Sciences, Beijing 101408, China. [3]Spallation Neutron Source Science Center, Dongguan 523803, China. [4]Institute of Sustainability for Chemicals, Energy and Environment, A*STAR (Agency for Science, Technology and Research), 1 Pesek Road, Jurong Island, Singapore 627833, Singapore.

*Address correspondence to: njutzhouyu@njtech.edu.cn (Y.Z.); junwang@njtech.edu.cn (J. W.)

Citation: Fu P, Meng B, Hu Q, Wei J, Yue Q, Sun M, Xu Q, Liu X, Xi S, Yin W, et al. Covalently Tethering Atomically Precise Au_{25} Nanoclusters onto Covalent Organic Framework for Visible-Light-Driven CO_2 Reduction. *Research* 2026;9:Article 1152. https://doi.org/10.34133/research.1152

Submitted 31 October 2025
Revised 11 January 2026
Accepted 27 January 2026
Published 27 February 2026

Copyright © 2026 Ping Fu et al. Exclusive licensee Science and Technology Review Publishing House. No claim to original U.S. Government Works. Distributed under a Creative Commons Attribution License (CC BY 4.0).

Solar-driven carbon dioxide (CO_2) reduction can sustainably produce chemicals and fuels but is often limited by rapid charge recombination and slow CO_2-to-product kinetics, typically necessitating homogeneous photosensitizers and cocatalysts. Here, we reported an integrated photocatalyst, TF-COF-CONH-Au_{25}-Co, constructed by immobilizing atomically precise Au_{25} nanoclusters (NCs) on a covalent organic framework (COF) incorporating $[Co(bpy)_3]^{2+}$ complex (Co–N_6 coordination). Under visible-light illumination, this hybrid catalyzes CO_2 conversion to syngas without external photosensitizers or cocatalysts, delivering a CO formation rate of 2,321.9 $\mu mol \cdot g^{-1} \cdot h^{-1}$ (turnover number of 171.9 and turnover frequency of 7.2 h^{-1}). The Au_{25} NCs enhance light responsiveness and charge transfer efficiency, thereby enriching long-lived photogenerated electrons, while concurrently modulating the electronic state of Co sites to reduce the energy barrier for CO_2 reduction. This study illustrates a molecular-level strategy to synergistically integrate metal NCs, COFs, and $[Co(bpy)_3]^{2+}$, showing a promising platform for high-performance photocatalytic CO_2 conversion.

Introduction

Solar-driven reduction of carbon dioxide (CO_2) represents a compelling strategy for addressing both climate change and global energy challenges [1–4]. Nevertheless, the formidable CO_2 thermodynamic stability and rapid charge recombination remain important obstacles to the development of efficient photocatalytic systems [5,6]. Homogeneous organometallic photosensitizers, typically Ru- or Re-based complexes, are normally involved in bridging the gap between sluggish CO_2 reduction kinetics and the short lifetimes of excited states [3,5,7]. Nevertheless, their high price, limited durability, and recycling difficulties restrict their practical application [8], making the urgent need for photosensitizer-free heterogeneous CO_2 photoreduction systems.

Atomically precise metal nanoclusters (NCs) are ligand-protected metal assemblies characteristic of well-defined chemical composition and structure [9–12]. Their subnanometer dimensions endow distinctive geometric and electronic properties, including abundant surface unsaturated sites, quantum confinement, and pronounced size effects [11,13–16]. In photocatalysis, the discrete energy level and the molecule-like behavior of metal NCs render excellent light harvesting across the ultraviolet–visible (UV–vis) near-infrared region [13,17,18]. They can function as narrow-bandgap semiconductors to generate photoexcited carriers and as the electron acceptors to suppress charge recombination [13,14,17]. However, their high surface free energy will easily lead to deactivation due to aggregation during the catalytic process [19,20]. Immobilization on well-defined porous supports via electrostatic interactions, encapsulation, coordination, or covalent bonding is therefore crucial to retain their structure and activity [20–24].

Covalent organic frameworks (COFs) are attractive supports due to the well-defined ordered porosity, tunable composition, ordered porosity, and predictable design [6,8,25–30]. Moreover, COF-based single-atom catalysts enable site-specific structural and functional control at the atomic level [8,31–34]. Here, we report the first example of immobilizing atomically precise $Au_{25}(Cys)_{18}$ NCs (Au_{25} NCs) on a COF scaffold bearing $[Co(bpy)_3]^{2+}$ complex. A 2-dimensional COF, named TF-COF, was synthesized via the condensation of 2,4,6-tris(4-formylphenyl)-1,3,5-triazine (TTA) and tris(4-formylphenyl)amine (TFA), followed by quinoline-4-carboxylic acid functionalization through an irreversible Doebner reaction to yield TF-COF-COOH [35,36]. Au_{25} NCs were covalently anchored through amidation between COF's carboxyl

groups and NCs' amino groups, affording TF-COF-CONH-Au_{25}. Subsequent incorporation of Co sites produced TF-COF-CONH-Au_{25}-Co. The Au NCs promote the light absorption and act as electron sinks to prolong carrier lifetimes. Meanwhile, their strong electronic interaction with neighboring Co sites modulates the local environment, thereby reducing the activation energy of the key step in CO_2 reduction. These synergistic effects enable TF-COF-CONH-Au_{25}-Co to drive visible-light-mediated CO_2 transformation into syngas, a valuable mixture of CO and H_2 that has numerous industrial applications [32,37], without extra photosensitizers or cocatalysts.

Results and Discussion

Construction of Au_{25} NCs tethered to COF

Figure 1 illustrated the overall strategy for the construction of Au_{25} NCs tethered to COFs, with the detailed synthetic route of the COF support shown in Fig. 2A. Au_{25} NCs were synthesized, and the structure was confirmed by UV–vis spectrum (Fig. S1) and high-resolution electrospray ionization mass spectrometry (Fig. S2) [20,38]. Powder x-ray diffraction (PXRD) analysis of TF-COF (Fig. 2B) displayed characteristic reflections at 4.39°, 7.66°, 8.88°, 11.74°, and 22.54°, indexing to the (100), (210), (200), (310), and (001) planes [39], respectively. TF-COF-COOH exhibited a nearly identical diffraction profile (Fig. 2C), indicating that the quinoline-4-carboxylic acid functionalization preserved the original COF framework. Simulated PXRD patterns based on an overlapping (AA) stacking model resembled the experimentally observed data (Fig. 2B and C and Figs. S3 and S4). Pawley refinements resulted in good agreement factors and provided the unit cell parameters (Fig. 2B and C). The chemical robustness of TF-COF-COOH was evaluated by exposure to harsh conditions, including strong base (3 M NaOH), strong acid (6 M HCl), oxidizing (0.5 M H_2O_2), and reducing (1 M $NaBH_4$) environments for 24 h. PXRD patterns validated the retention of crystallinity (Fig. 2D), whereas TF-COF suffered framework collapse under the same treatments (Fig. S5), demonstrating that conversion of imine linkages to quinoline units enhanced chemical stability. Importantly, TF-COF-CONH-Au_{25} exhibited a PXRD pattern essentially identical to TF-COF-COOH (Fig. S6), verifying that covalent anchoring of Au_{25} NCs did not disrupt the COF lattice.

Fourier transform infrared (FT-IR) spectrum of TF-COF showed a characteristic band at 1,626 cm^{-1}, assignable to the C═N stretching vibration of the imine unit (Fig. S7A) [40,41]. This band disappeared in TF-COF-COOH and TF-COF-CONH-Au_{25}, accompanied by new absorptions at 1,722 and 1,608 cm^{-1}, attributable to the C═O stretching of the quinoline-4-carboxylic acid moiety and the pyridyl group vibration [35,36], respectively. The C═O peak in the spectrum of TF-COF-CONH-Au_{25} was red-shifted relative to TF-COF-COOH (Fig. S7B), indicative of the amide bond generation [42,43]. Solid-state ^{13}C nuclear magnetic resonance (NMR) spectra confirmed the structural transformation (Figs. S8 to S10). TF-COF displayed a resonance at 157 parts per million (ppm) from imine carbon, which disappeared in TF-COF-COOH, alongside the emergence of a –COOH signal at 172 ppm [35,36]. TF-COF-CONH-Au_{25} showed a C═O resonance at 174 ppm from the amide linkage and an additional peak at 64 ppm assignable to the methylene group of the Au_{25} NC ligand (Fig. S10). Nitrogen sorption measurement revealed the type I isotherms for TF-COF and TF-COF-COOH (Fig. S11A) [44]. The surface areas were 1,510 and 1,215 $m^2 \cdot g^{-1}$, respectively, with the most probable pore sizes of 21 Å (Fig. S11B and Table S1). TF-COF-CONH-Au_{25} exhibited a type IV isotherm with a reduced surface area of 640 $m^2 \cdot g^{-1}$, consistent with partial pore occupancy by bulky Au_{25} NCs. CO_2 sorption

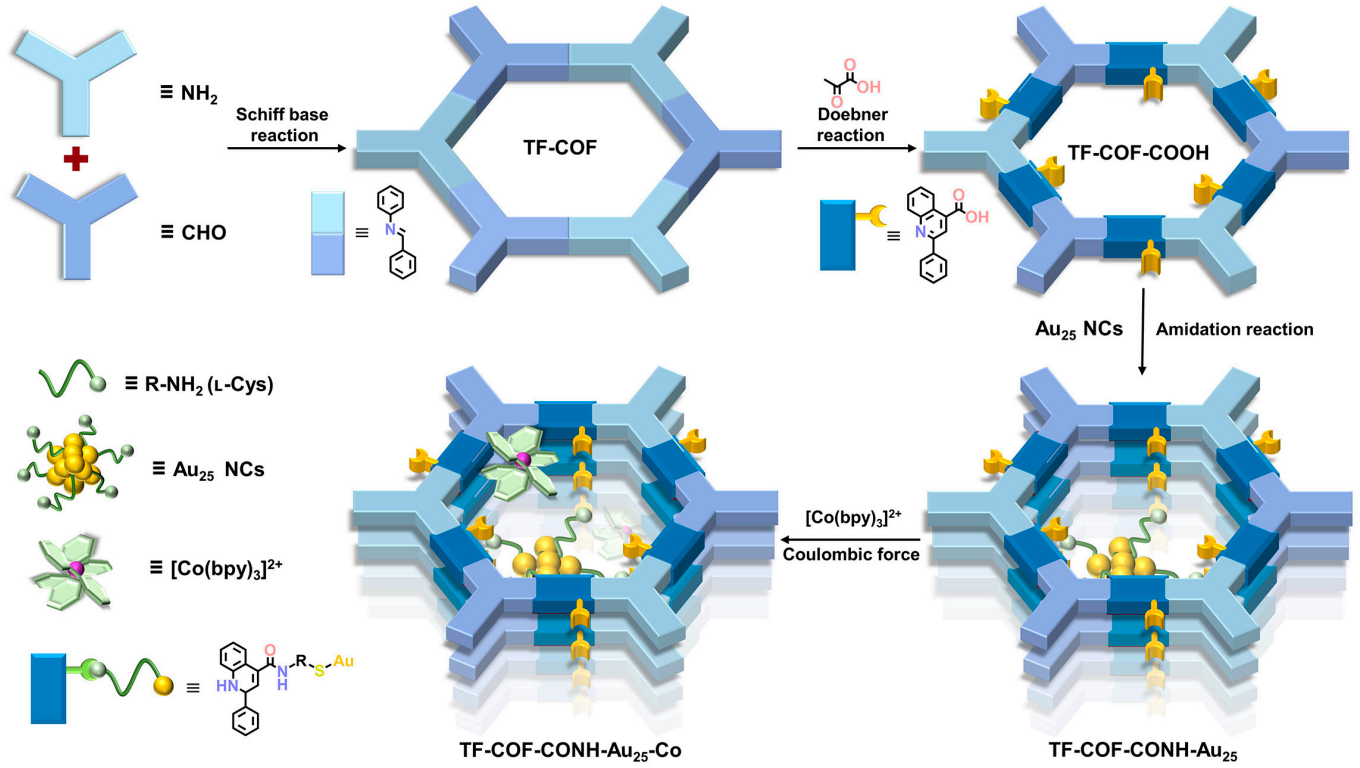


Fig. 1. Synthesis schematic diagram. Schematic illustration showing the integration of Au_{25} NCs, COFs, and $[Co(bpy)_3]^{2+}$ complex.

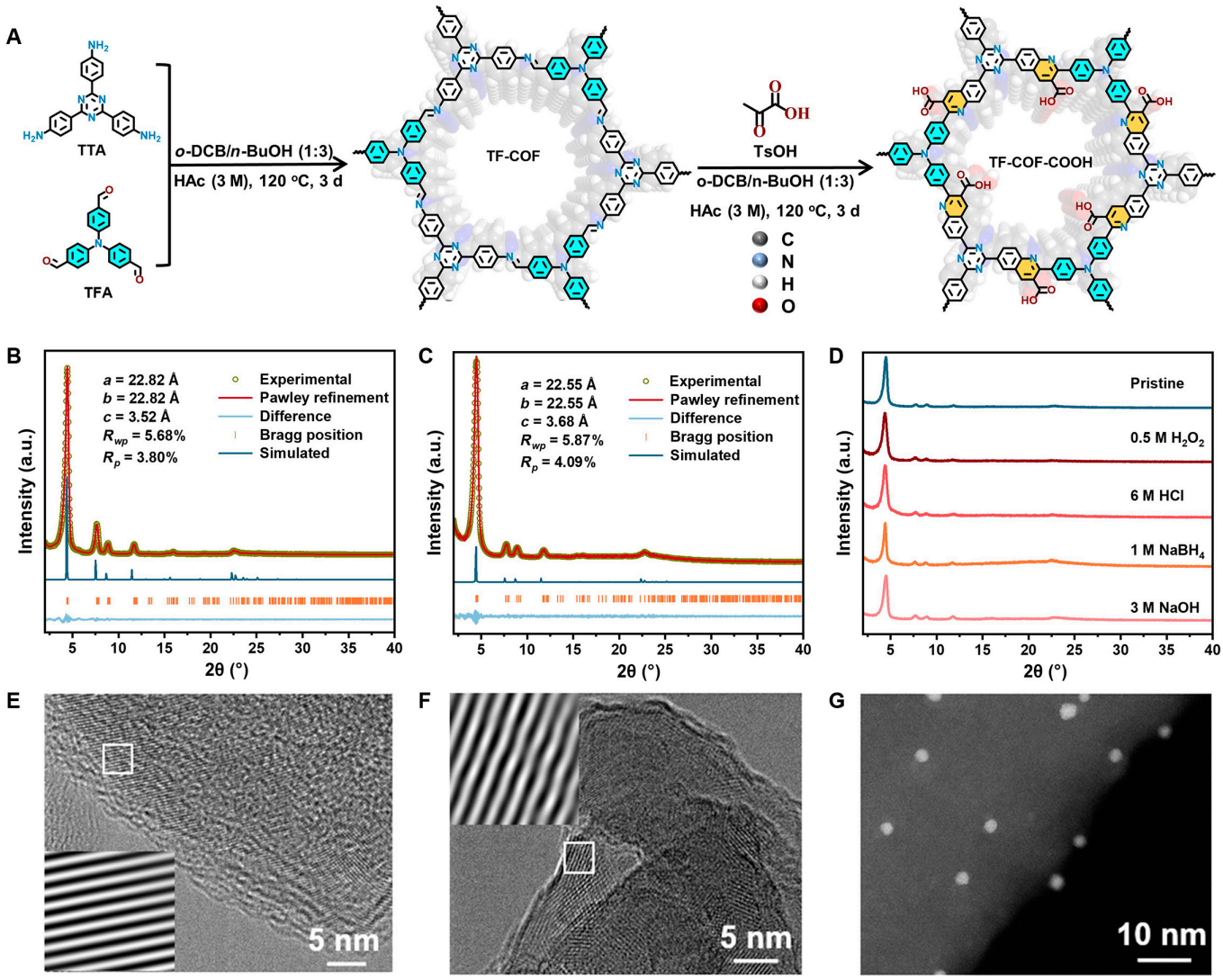


Fig. 2. Crystal structure and morphology. (A) Synthetic procedure of TF-COF and TF-COF-COOH. *o*-DCB, *ortho*-dichlorobenzene; *n*-BuOH, *n*-butanol; HAc, acetic acid. PXRD patterns and Pawley refinements of (B) TF-COF and (C) TF-COF-COOH. a.u., arbitrary units. (D) PXRD patterns of TTA-TFA-COOH after treatment in 3 M NaOH, 6 M HCl, 1 M $NaBH_4$, and 0.5 M H_2O_2 for 1 d. High-resolution TEM images of (E) TF-COF and (F) TF-COF-CONH-Au_{25}. (G) HAADF-STEM image of TF-COF-CONH-Au_{25}.

isotherms at 298 K demonstrated that the uptake at 1 bar increased from 36.7 $cm^3 \cdot g^{-1}$ for TF-COF to 48.6 and 41.4 $cm^3 \cdot g^{-1}$, respectively, for TF-COF-COOH and TF-COF-CONH-Au_{25} (Fig. S12). The Au content in TF-COF-CONH-Au_{25} was approximately 5.56 wt %. Scanning electron microscopy (SEM) images of these COFs showed similar coral-bar morphology (Fig. S13), while elemental imaging confirmed homogeneous distribution of C, N, O, S, and Au in TF-COF-CONH-Au_{25} (Fig. S14). Transmission electron microscopy (TEM) images of TF-COF and TF-COF-COOH revealed well-resolved lattice fringes, indicative of high crystallinity (Fig. 2E and F). High-angle annular dark-field scanning TEM (HAADF-STEM) and TEM images of TF-COF-CONH-Au_{25} visualized uniformly distributed NCs (Fig. 2G and Fig. S15), confirming the incorporation of Au_{25} NCs.

X-ray photoelectron spectroscopy (XPS) was conducted to elucidate the surface chemical states (Figs. S16 to S20). The survey scan XPS spectra revealed the C 1s, N 1s, and O 1s signals at 291.4, 404.4, and 540.1 eV, respectively, while TF-COF-CONH-Au_{25} exhibited additional Au 4f (87.0 eV) and S 2p (162.0 eV) peaks (Fig. S16) [20,42]. High-resolution N 1s XPS spectra (Fig. S17) corroborated the integration of quinoline-4-carboxylic acid units in both TF-COF-COOH and TF-COF-CONH-Au_{25}, with a characteristic quinoline nitrogen signal at 400.2 eV, alongside contributions from sp^3-N (399.3 eV) and imine/triazine nitrogen (C=N; 400.3 eV) [39]. TF-COF-CONH-Au_{25} exhibited an extra component at 401.7 eV from the amide nitrogen [20]. The C 1s and O 1s spectra (Figs. S18 and S19) of TF-COF-COOH and TF-COF-CONH-Au_{25} presented the peaks at 288.8 and 532.4 eV, respectively, arising from the –COOH moieties [35,36]. The Au 4f and S 2p peaks of TF-COF-CONH-Au_{25} showed a positive binding energy shift compared to pristine Au_{25} NCs (Fig. S20), suggesting reduced electron densities on Au and S atoms due to the NC–COF interaction [20].

The local metal coordination environment was measured by x-ray absorption fine structure (XAFS) analysis (Fig. 3A to F). The Au L_3-edge x-ray absorption near-edge structure (XANES) spectrum of TF-COF-CONH-Au_{25} displayed a rising edge of TF-COF-CONH-Au_{25} close to that of Au foil (Fig. 3A), indicating that the Au_{25} NCs in TF-COF-CONH-Au_{25} retained

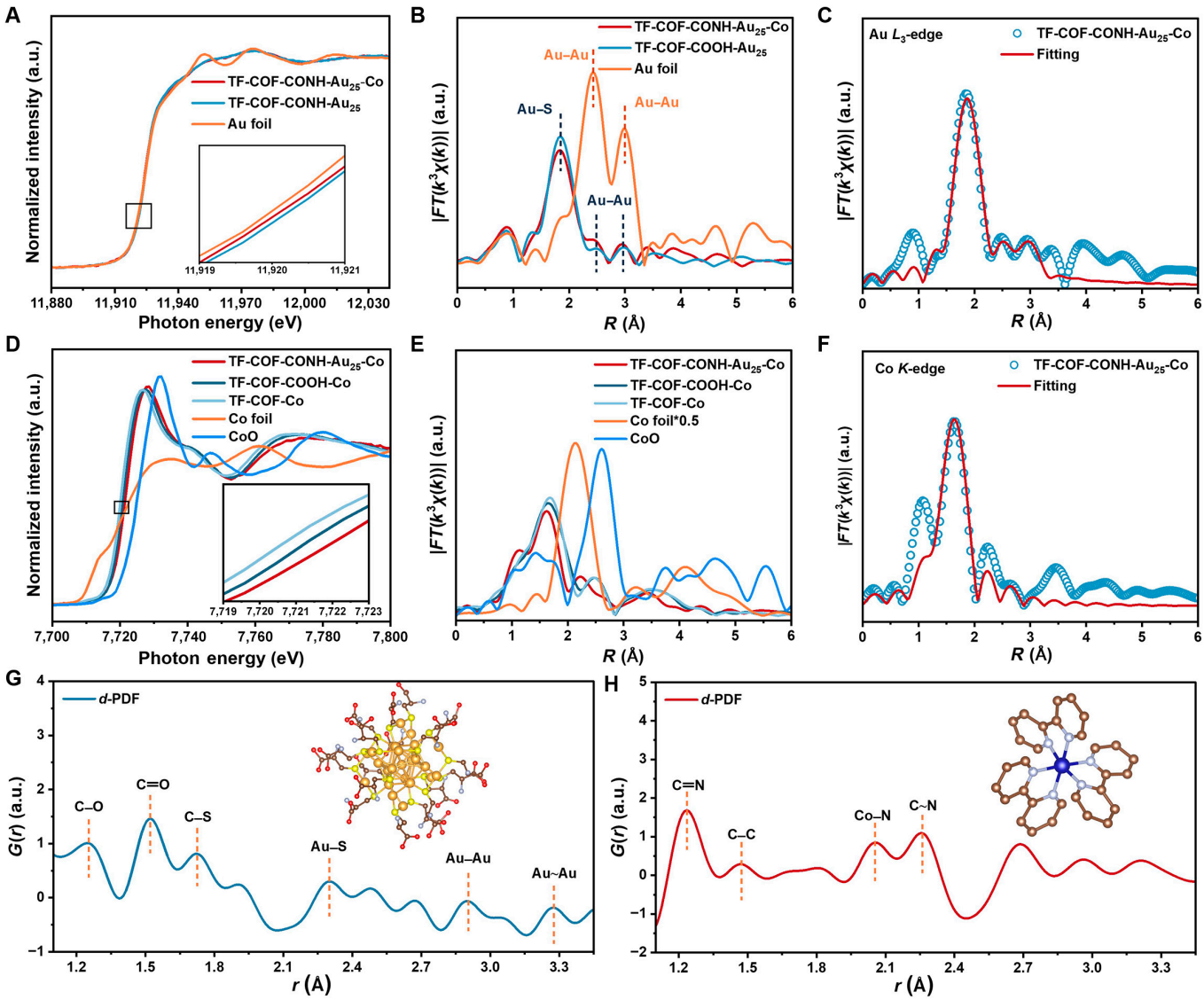


Fig. 3. EXAFS spectra and neutral scattering. (A) XANES and (B) FT-EXAFS spectra at the Au L_3-edge of TF-COF-CONH-Au_{25}, TF-COF-CONH-Au_{25}-Co, and Au foil. (C) EXAFS fitting curves at the Au L_3-edge of TF-COF-CONH-Au_{25}-Co. (D) XANES and (E) FT-EXAFS spectra at the Co *K*-edge of TF-COF-CONH-Au_{25}-Co, TF-COF-COOH-Co, TF-COF-Co, Co foil, and CoO. (F) EXAFS fitting curves at the Co *K*-edge of TF-COF-CONH-Au_{25}-Co. (G) *d*-PDF profile between TF-COF-CONH-Au_{25} and TF-COF-COOH. (H) *d*-PDF between TF-COF-CONH-Au_{25}-Co and TF-COF-CONH-Au_{25}. Blue data points and solid lines in (C) and (F) represent the experimental values and fitting values for TF-COF-CONH-Au_{25}-Co, respectively.

a metallic state with a slight positive charge [45]. Fourier-transformed L_3-weighted extended XAFS (FT-EXAFS) spectrum of TF-COF-CONH-Au_{25} (Fig. 3B) demonstrated a dominant peak at 1.8 Å for Au–S coordination in the outermost layer of Au_{25} NCs [46]. Two weak peaks were observed at 2.5 and 3.0 Å for Au–Au contribution in the inner core of Au_{25} NCs [46,47]. Multishell EXAFS fitting (Fig. 3C, Figs. S21 to S23, and Table S2) displayed Au–S coordination number (CN) of 1.6 at 2.3 Å and Au–Au CNs of 1.5 (2.8 Å), 1.6 (3.1 Å), and 1.9 (3.3 Å) in TF-COF-CONH-Au_{25}, consistent with reported structures of Au_{25} NCs [48,49].

Neutron total scattering combined with pair distribution function (PDF) analysis was performed on TF-COF-COOH and TF-COF-CONH-Au_{25} to gain atomic-level structure insights [32,50]. Covalent bonding of Au_{25} NCs intensified several peaks and introduced new features in the PDF profiles (Fig. 3G and Figs. S24 to S26). Differential neutron PDF (*d*-PDF) was obtained by subtracting the neutron PDF of TF-COF-COOH from TF-COF-CONH-Au_{25}, showing the correlations at $r = 1.3$, 1.5, 1.7, 2.3, 2.9, and 3.3 Å for C–O, C=C, C=S, Au–S, Au–Au, and Au~Au (inner core Au_{13} to outer Au atoms), respectively. The experimentally obtained *d*-PDF profile agreed with the refined one (Figs. S25 and S26), confirming the covalent tethering and structural integrity of the Au_{25} NCs within the COF frameworks.

Anchoring of $[Co(bpy)_3]^{2+}$ complex

Co species were anchored by complexing the COFs with $[Co(bpy)_3]^{2+}$ cations via Coulombic interaction and pore confinement (Fig. 1) [51,52]. Zeta potential tests revealed that the potentials of TF-COF, TF-COF-COOH, and TF-COF-CONH-Au_{25} were negatively charged, while $[Co(bpy)_3]^{2+}$ exhibited a positive potential of +18.2 mV (Fig. S27), enabling their assembly through electrostatic attraction. The resulting TF-COF-CONH-Au_{25}-Co had a Co loading of 1.91 wt %, while TF-COF-Co and TF-COF-COOH-Co exhibited a Co content of 1.76 and 2.13 wt %, respectively. PXRD, FT-IR, nitrogen

sorption, and SEM analyses verified the preservation of crystalline structure, porosity, and morphology (Figs. S28 to S31). TEM image verified the existence of Au NCs (Fig. S32).

Survey scan XPS spectra revealed the Au and Co signals (Fig. S33). High-resolution Au 4f XPS spectra showed a negative shift of the Au 4f signals of TF-COF-CONH-Au_{25}-Co relative to TF-COF-CONH-Au_{25} (Fig. S34), reflecting the decrease in the valence state of Au species due to the interaction between Co species and Au_{25} NCs [17]. High-resolution Co 2p XPS spectrum of COF-CONH-Au_{25}-Co displayed peaks at 797.4 and 781.4 eV, confirming Co(II) species (Fig. S35) [53]. The Co 2p signals of TF-COF-COOH-Co and TF-COF-CONH-Au_{25}-Co were red-shifted relative to TF-COF-Co, revealing a higher Co oxidation state (Fig. S35). XANES analysis further supported these findings. The Au L_3-edge profile of TF-COF-CONH-Au_{25}-Co resembled that of TF-COF-CONH-Au_{25} (Fig. 3A), with a slight negative shift suggesting reduced Au valence [54], while the Au coordination environment remained unchanged, confirming the structural integrity of Au_{25} NCs. In the Co *K*-edge XANES (Fig. 3D), the absorption edges of TF-COF-Co, TF-COF-COOH-Co, and TF-COF-CONH-Au_{25}-Co align closely with CoO, indicating Co valence near +2. The subtle edge shifts were attributable to ligand-field/covalency differences from bpy-N coordination. A weak pre-edge at ~7,707 eV further supported a distorted octahedral Co(II), consistent with the Co 2p XPS result [55,56]. The Co valence increased in the sequence of TF-COF-Co < TF-COF-COOH-Co < TF-COF-CONH-Au_{25}-Co, reflecting enhanced Co–COF interactions promoted by –COOH groups and Au_{25} NCs (Figs. S36 and S37) [55,57,58]. FT-EXAFS spectra of these Co-loaded COFs exhibited the Co–N contribution at 1.6 Å (Fig. 3E). No distinct peak corresponding to the Co–Co coordination was observed at ~2.1 Å, reflecting the atomically dispersed Co species [59,60]. EXAFS fitting gave the CN of ~6 and bond length of 2.1 Å for Co–N contribution (Fig. 3F, Figs. S38 to S42, and Table S3). The *d*-PDF profiles of TF-COF-CONH-Au_{25} and TF-COF-CONH-Au_{25}-Co showed the presence of correlations at r = 1.3, 1.5, 2.1, and 2.3 Å, respectively, for C=N, C–C, Co–N, and C~N (pyridyl C–N) of loaded $[Co(bpy)_3]^{2+}$. This result revealed the existence of immobilized $[Co(bpy)_3]^{2+}$, which is further confirmed by the good match between the refined *d*-PDF profile and the experimentally obtained one (Fig. 3H and Figs. S43 to S45).

Photocatalytic CO_2 reduction

We performed the photocatalytic CO_2 conversion under visible light irradiation (≥400 nm). TF-COF-CONH-Au_{25}-Co demonstrated outstanding activity, continuously generating syngas (CO + H_2) with linear product accumulation over time (Fig. 4A and Figs. S46 to S49). CO and H_2 were produced at rates of 2,321.9 and 1,717.4 μmol·g^{-1}·h^{-1}, respectively, corresponding to the turnover number (TON) and turnover frequency (TOF) of 171.9 and 7.2 h^{-1} for CO generation. An ~1- to 2-h induction preceded steady state, arising from photoactivation of Co centers and triethanolamine (TEOA)-assisted charge separation build-up, as evidenced by the reversible growth of a 500- to 700-nm band in quasi in situ UV–vis spectra (Figs. S46 and S47) [61]. By contrast, TF-COF-COOH-Co achieved CO and H_2 production rates of 1,042.7 and 124.8 μmol·g^{-1}·h^{-1}, respectively, while

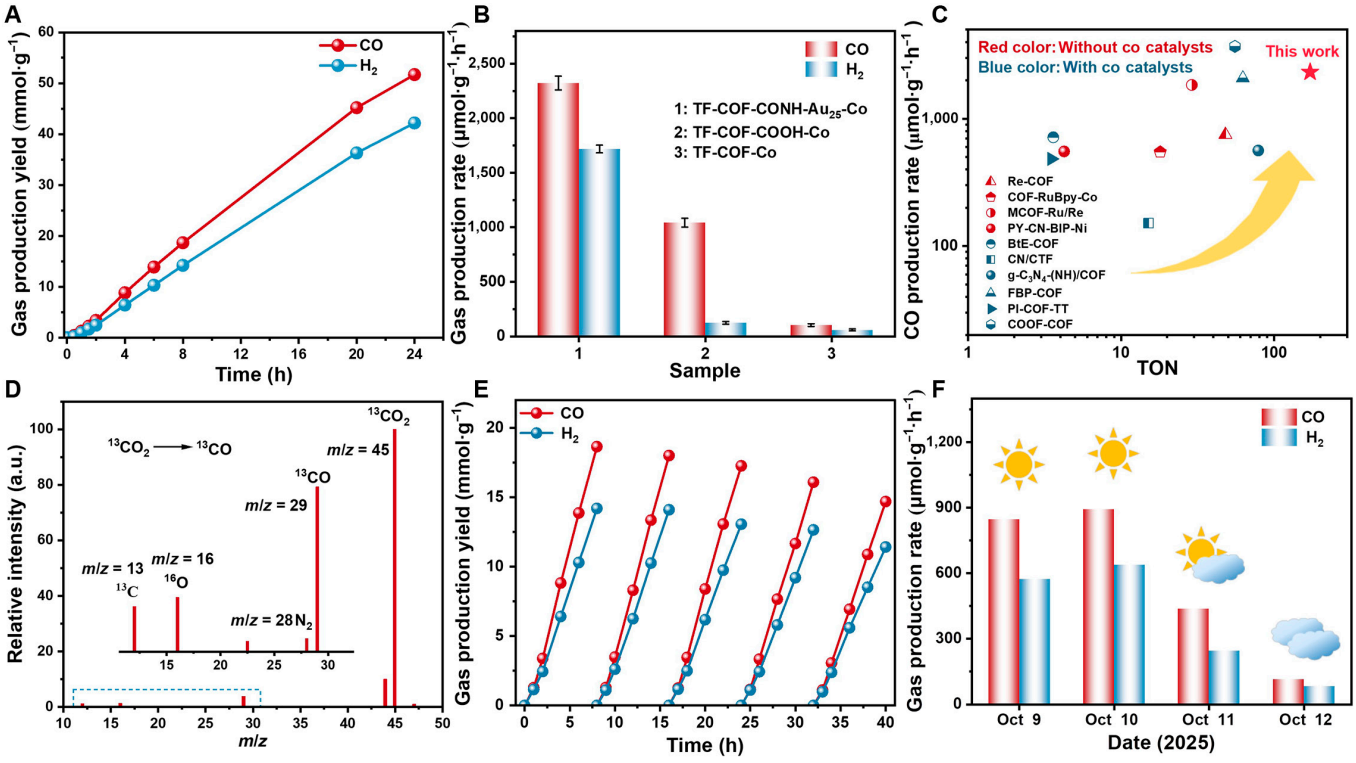


Fig. 4. Photocatalytic performance. (A) Time-resolved generation of gas (CO and H_2) over TF-COF-CONH-Au_{25}-Co in 24 h. (B) Gas (CO and H_2) production rates of TF-COF-Co, TF-COF-COOH-Co, and TF-COF-CONH-Au_{25}-Co. (C) Comparison of TF-COF-CONH-Au_{25}-Co with representative COF-based photocatalysts for CO_2-to-CO conversion under visible-light irradiation without photosensitizers. The plot compares CO evolution rates and TON of reported photosensitizer-free COF systems, highlighting the superior performance of TF-COF-CONH-Au_{25}-Co. (D) Mass spectrum of the gaseous product in TF-COF-CONH-Au_{25}-Co-catalyzed $^{13}CO_2$ conversion. (E) Recyclability of TF-COF-CONH-Au_{25}-Co. (F) The photocatalytic CO production rate of TF-COF-CONH-Au_{25}-Co under natural sunlight.

TF-COF-Co exhibited minimal activity (103.9 μmol·g^{-1}·h^{-1} for CO and 60.4 μmol·g^{-1}·h^{-1} for H_2) (Fig. 4B). The superior performance of TF-COF-CONH-Au_{25}-Co highlighted the synergy of Au_{25} NCs and Co centers. The inertness of Co-free analogs (TF-COF, TF-COF-COOH, and TF-COF-CONH-Au_{25}) confirmed that Co species served as the active sites (Fig. S50). Au_{25} NCs produced no detectable CO and only trace H_2 (76 μmol·g^{-1}·h^{-1}; Fig. S51), excluding Au_{25} as a carbon dioxide reduction reactioin (CO_2RR) site. The physically mixed Au_{25}+TF-COF-CONH-Co delivered a lower CO production rate of 1,313.0 μmol·g^{-1}·h^{-1} (Fig. S51), underscoring that covalent tethering is critical for efficient interfacial charge transfer. The apparent quantum yield for TF-COF-CONH-Au_{25}-Co reached 0.58% at 400 nm (Fig. S52). A comprehensive comparison with previous photosensitizer-free systems under comparable reaction conditions revealed that TF-COF-CONH-Au_{25}-Co is advanced in terms of CO production rate, TON, and TOF (Fig. 4C and Table S4) [29,51,52,55,59,62].

Control experiments further verified the reaction pathway (Fig. S53). Certain H_2 and trace CO were detected without the sacrificial agents. No product was detectable under dark conditions, illustrating the light dependence. Ar atmosphere led to the sole H_2 production, suggesting the formation of CO from CO_2. Photoreduction of $^{13}CO_2$ (Fig. 4D) caused the formation of ^{13}CO, as demonstrated by the ^{13}CO signal (mass/charge ratio $[m/z] = 29$) in gas chromatography–mass spectrometry, substantiating CO_2 as the carbon source [63]. ^1H NMR spectrum excluded the generation of potential liquid products (Fig. S54). Over 5 consecutive 8-h cycles (40 h total), COF-CONH-Au_{25}-Co sustained a CO rate of 1,798.8 μmol·g^{-1}·h^{-1} (~77% retention; Fig. 4E). Postreaction PXRD of the recovered catalyst showed intact COF reflections without peak broadening or shifts (Fig. S55), while XPS confirmed preservation of the Au^0 $4f_{7/2}$ and Co^{2+} $2p_{3/2}$ features and the absence of new oxide signatures (Fig. S56). Inductively coupled plasma mass spectrometry showed the recovered catalyst retained 1.62 wt % Co (~85% of the starting 1.91 wt %), showing only minor leaching and quite robust immobilization of Co complex. By contrast, the physically mixed Au_{25}+TF-COF-CONH-Co exhibited poorer activity retention (Fig. S57), indicating that covalent anchoring markedly enhances durability. In addition, we further evaluated the photocatalytic performance of TF-COF-CONH-Au_{25}-Co under natural sunlight (Fig. 4F). The CO and H_2 production rate depended on the weather conditions, exhibiting the highest activity (891.6 and 637.5 μmol·g^{-1}·h^{-1} for CO and H_2) on 2025 October 10, a sunny day.

Photoelectrochemical properties

We systematically evaluated the photoelectrochemical properties of TF-COF, TF-COF-COOH, TF-COF-CONH-Au_{25}, and their Co-loaded analogs. UV–vis spectra revealed that the introduction of 4-carboxyquinoline units into TF-COF induced a red shift in the absorption edge (Fig. 5A), attributed to enhanced π-conjugation [35,62]. The optical bandgap energy (E_g) changed from 2.38 eV for TF-COF to 1.95 eV for TF-COF-COOH and 1.86 eV for TF-COF-CONH-Au_{25} (Figs. S58 and S59). Mott–Schottky analysis indicated n-type semiconducting behavior for all 3 COFs, with conduction band (CB) potentials of −0.86, −0.99, and −1.12 V versus the normal hydrogen electrode (NHE) [64], sufficiently negative for CO_2-to-CO transformation (−0.53 V versus NHE) (Figs. S60 to S63) [32,40]. Co loading resulted in little effect on the band alignment but slightly enhanced visible-light absorption (Fig. 5A and Fig. S59).

Steady-state photoluminescence (PL) spectra showed a pronounced emission for TF-COF, while TF-COF-COOH, TF-COF-CONH-Au_{25}, and TF-COF-CONH-Au_{25}-Co demonstrated progressively quenched signals, reflecting the inhibited radiative recombination (Fig. 5B) [62]. Time-resolved PL spectra revealed prolonged carrier lifetimes by introducing –COOH (1.42 ns) and Au_{25} NCs (1.44 ns) relative to TF-COF (1.29 ns), with the longest lifetime for TF-COF-CONH-Au_{25}-Co (1.68 ns) (Fig. 5C and Table S5) [20,35,62]. Transient surface photovoltage (TPV) measurements showed an increasing trend in both signal intensity and accumulated charge (A) from TF-COF to TF-COF-CONH-Au_{25}-Co, along with shorter charge extraction times (T_{max}) and larger decay constants (τ), with τ increasing from 0.104 μs (TF-COF) to 1.140 μs (TF-COF-CONH-Au_{25}-Co) (Fig. 5D to F and Table S6), suggesting a obviously reduced recombination rate [65,66]. Electrochemical impedance spectroscopy (EIS) spectra showed the smallest semicircle for TF-COF-CONH-Au_{25}-Co, corresponding to the lowest charge transfer resistance (Fig. S64) [28,55,67]. The photocurrent density followed the order of TF-COF < TF-COF-COOH < TF-COF-CONH-Au_{25} < TF-COF-CONH-Au_{25}-Co (Fig. S65), in agreement with the improved charge separation and transport efficiency [55,62].

The photoelectrochemical properties of the other 2 Co-loaded materials, TF-COF-Co and TF-COF-COOH-Co, were compared with each parent COF. Co loading enhanced the charge separation and transfer as shown by the declined peak intensity in the PL spectra, extended carrier decay lifetime in the time-resolved PL spectra, increased TPV peak intensity, elongated decay constants, declined charge transfer resistance, and boosted photocurrent response (Figs. S66 to S70 and Tables S5 and S6) [55,68,69]. All these measurements indicate that the cooperation of Au_{25} NCs, COFs, and Co sites enhances light harvesting, facilitates charge separation and transfer, and thereby provides an abundance of long-lived photoelectrons.

Femtosecond transient absorption (fs-TA) spectra were collected to investigate the electron transfer dynamics. All samples exhibited a broad negative bleaching signal, indicative of ground-state bleaching, suggesting the excitation of carriers leading to exciton formation (Fig. 5G and H and Figs. S71 to S73). As the probe time progressed, this negative bleaching signal gradually transitioned into an excited-state absorption (ESA) signal, indicating the occurrence of charge transfer processes. Notably, TF-COF-CONH-Au_{25}-Co displayed a obviously stronger ESA signal than TF-COF-CONH-Au_{25}, TF-COF-COOH, and TF-COF [70]. Global fits to the TA kinetics resolved biexponential decays for TF-COF, TF-COF-COOH, and TF-COF-CONH-Au_{25} and a triexponential response for TF-COF-CONH-Au_{25}-Co (Fig. 4I, Figs. S74 to S76, and Table S7) [71]. We assigned the fast component (τ_1) to electron diffusion/dissociation within the COF domain and the slower component (τ_2) to trap-assisted recombination [56,72]. TF-COF showed $\tau_1 = 3.99$ ps ($k_1 \approx 2.5 \times 10^{11}$ s^{-1}) and $\tau_2 = 365.2$ ps ($k_2 \approx 2.7 \times 10^{9}$ s^{-1}), while carboxylation modestly lengthens both τ_1 (4.89 ps) and τ_2 (437.6 ps) over TF-COF-COOH, consistent with slightly improved carrier separation [33]. Incorporating Au_{25} further extended lifetimes ($\tau_1 = 5.87$ ps and $\tau_2 = 518.9$ ps), indicating efficient exciton harvesting by the cluster yet recombination that still dominates on the subnanosecond scale in the absence of Co. By contrast, TF-COF-CONH-Au_{25}-Co exhibited $\tau_1 = 0.93$ ps ($k_1 \approx 1.1 \times 10^{12}$ s^{-1}), $\tau_2 = 34.3$ ps ($k_2 \approx 2.9 \times 10^{10}$ s^{-1}), and an emergent long-lived component $\tau_3 = 982.3$ ps ($k_3 \approx 1.0 \times 10^{9}$ s^{-1}). We attributed these to ultrafast COF → Au_{25} exciton capture (τ_1), rapid Au_{25} → Co electron relay

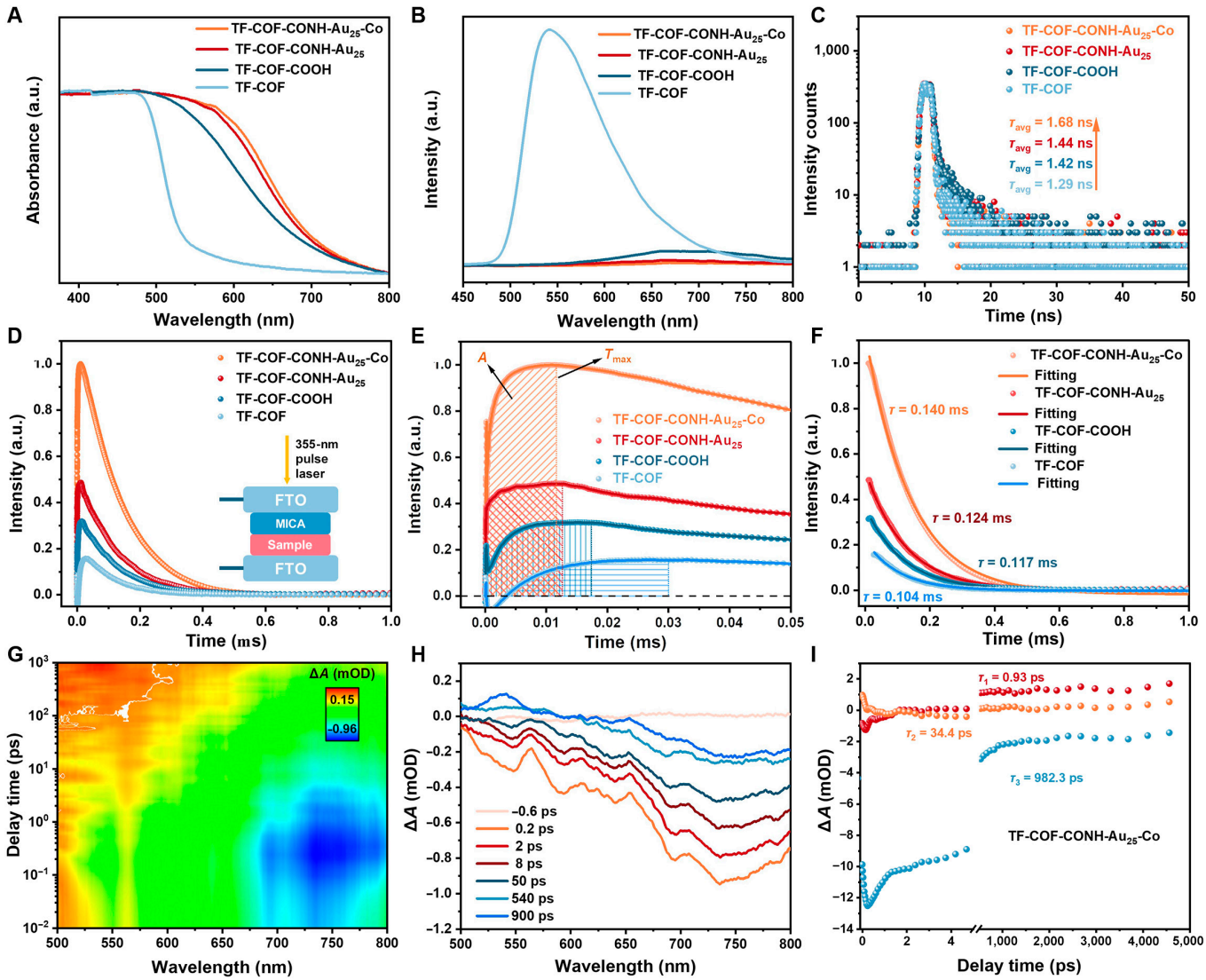


Fig. 5. Photoelectrochemical properties. (A) UV–vis spectra, (B) PL spectra, (C) time-resolved PL decay spectra for TF-COF, TF-COF-COOH, TF-COF-CONH-Au_{25}, and TF-COF-CONH-Au_{25}-Co. (D) TPV curves, (E) maximum charge extraction time (T_{max}), and (F) attenuation constants (τ) for TF-COF, TF-COF-COOH, TF-COF-CONH-Au_{25}, and TF-COF-CONH-Au_{25}-Co. FTO, fluorine-doped tin oxide. Light blue, dark blue, red, and orange data points and solid lines in (F) represent the experimental and fitting values for TF-COF, TF-COF-COOH, TF-COF-CONH-Au_{25}, and TF-COF-CONH-Au_{25}-Co, respectively. (G) 2D mapping TA spectra and (H) fs-TA spectra of TF-COF-CONH-Au_{25}-Co at different decay times. (I) Representative kinetic traces along with their global fitting results of the fs-TA spectra of TF-COF-CONH-Au_{25}-Co. mOD, milliopital density.

and stabilization at the cobalt center (τ_2), and a persistent charge-separated state (τ_3) that suppresses recombination [72]. Thus, covalent integration of Au_{25} (electron sink) with Co sites transforms a 4- to 6-ps/300- to 500-ps exciton recombination sequence into subpicosecond harvesting, tens-of-picosecond interfacial transfer, and ~1-ns charge separation, quantitatively accounting for the stronger time-resolved PL quenching, reduced EIS semicircles/TPV shifts, and higher CO formation rates.

In situ spectral and theoretical study

Quasi in situ XPS spectra of TF-COF-CONH-Au_{25}-Co under light irradiation (Fig. 6A) indicated that the Au 4f level underwent a −0.5 eV shift, whereas the Co 2p level shifted by +0.3 eV (Fig. 6B). The negative shift on Au signifies transient electron accumulation, while the positive shift on Co indicates electron depletion (upward band bending), collectively evidencing a directional, light-driven COF → Au_{25} → Co electron-transfer cascade [73,74].

Photochromism further corroborated carrier generation and shuttling. Dispersions of TF-COF-CONH-Au_{25} in acetonitrile (MeCN)/TEOA/1,3-dimethyl-2-phenyl-2,3-dihydro-1*H*-benzo[d]imidazole (BIH) turned yellow to green under light. In situ electron paramagnetic resonance (EPR) revealed a strong growth of the paramagnetic signal after illumination (Fig. 6C). In contrast, the EPR intensity diminished when $[Co(bpy)_3]^{2+}$ is present (TF-COF-CONH-Au_{25}-Co), indicating electron transfer from the COF/Au_{25} ensemble to the Co complex with the reduction of Co sites [75,76]. Cyclic voltammetry resolved 2 irreversible reductions assignable to $[Co(bpy)_3]^{2+} \rightarrow [Co(bpy)_2]^{+}$ and $[Co(bpy)_2]^{+} \rightarrow [Co^{I}(bpy)(bpy)^{\bullet-}]$. Currents were enhanced under CO_2 versus Ar, consistent with engagement of the reduced Co species in CO_2 activation (Fig. S77) [55,56].

In situ attenuated total reflection surface enhanced infrared absorption spectroscopy (ATR-SEIRAS) measurements were used to track the CO_2 photoreduction pathway over TF-COF-CONH-Au_{25}-Co (Fig. 6D). Characteristic bands at 1,721 and 1,402 cm^{-1}

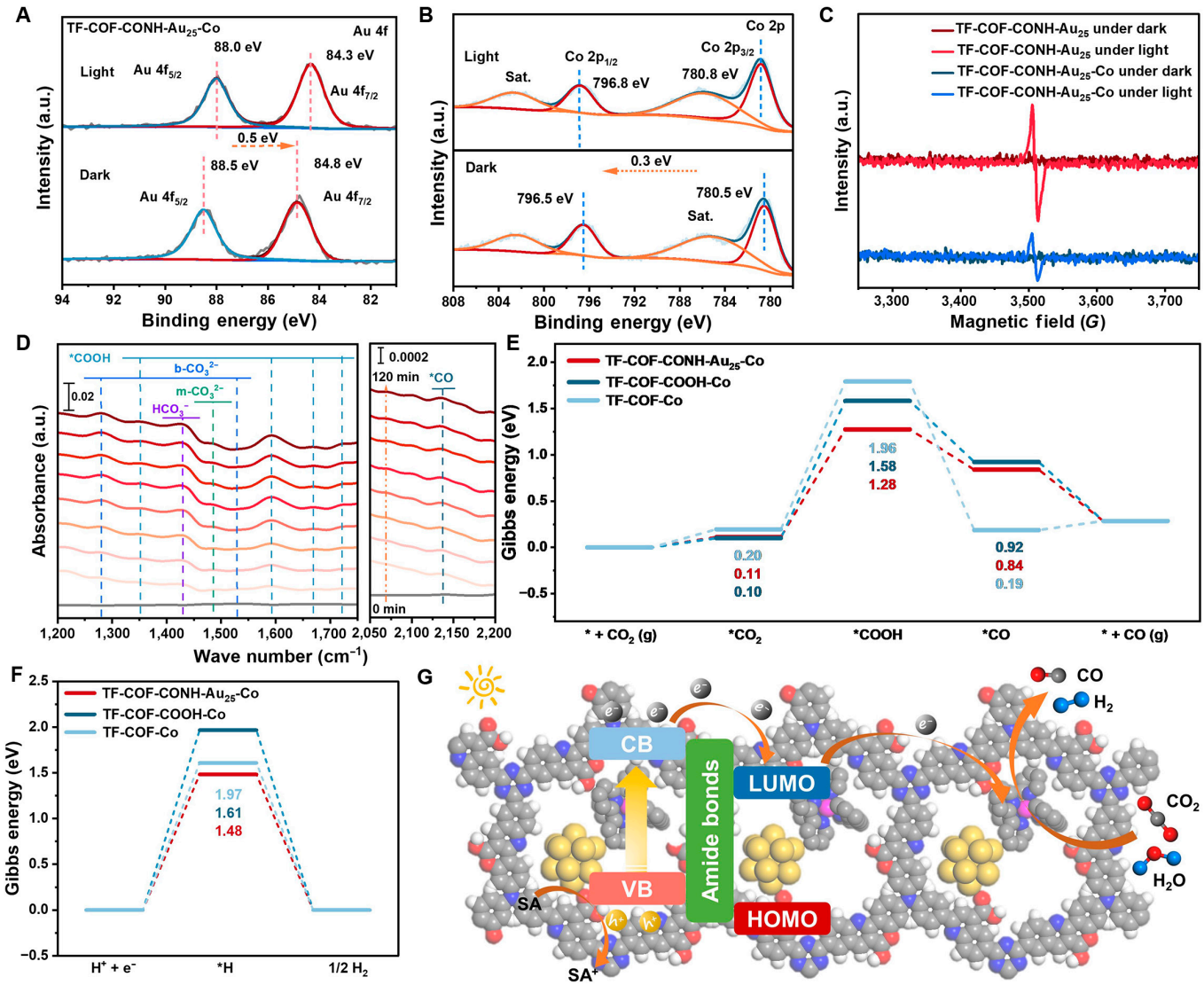


Fig. 6. In situ spectral and theoretical study. Quasi in situ (A) Au 4f and (B) Co 2p XPS spectra of TF-COF-CONH-Au_{25}-Co in the dark or under visible light illumination. (C) In situ EPR spectra of TF-COF-CONH-Au_{25} (red) and TF-COF-CONH-Au_{25}-Co (blue) in MeCN/TEOA/BIH under dark and visible-light illumination. (D) In situ ATR-SEIRAS for the adsorption and photocatalytic conversion of CO_2 on TF-COF-CONH-Au_{25}-Co. Gibbs free energy profiles (ΔG, in electron volts) of (E) CO generation and (F) H_2 evolution on TF-COF-Co, TF-COF-COOH-Co, and TF-COF-CONH-Au_{25}-Co. (G) Photocatalytic CO_2 conversion over TF-COF-CONH-Au_{25}-Co. VB, valence band; HOMO, highest occupied molecular orbital; SA, sacrificial agent.

were assignable to HCO_3^-, formed via coadsorption of CO_2 and H_2O [41]. Signals at 1,669, 1,593, and 1,352 cm^{-1} corresponded to the *COOH intermediate [77], while additional peaks at 1,559/1,281 cm^{-1} and 1,531/1,486 cm^{-1} indicated bidentate (b-CO_3^{2-}) [78] and monodentate (m-CO_3^{2-}) [37,79]. A distinct band at 2,134 cm^{-1} was assignable to *CO [34,79]. The gradual increase in peak intensities with irradiation time confirmed continuous formation of these intermediates, supporting a reaction sequence of CO_2 adsorption, *COOH generation, *CO formation, and CO release. The Co-free control (TF-COF-CONH-Au_{25}) showed only bicarbonate/carbonate signals (no *COOH/*CO; Fig. S78), whereas TF-COF-COOH-Co (no Au_{25}) exhibited the same assignment but with lower *COOH/*CO intensities (Fig. S79). Together with EPR, these results establish Co complexes as the catalytic reduction sites and demonstrate that Au_{25} funnels electrons to Co, amplifying intermediate coverage and turnover.

Theoretical study using density functional theory (DFT) was conducted on representative frameworks of TF-COF-Co, TF-COF-COOH-Co, and TF-COF-CONH-Au_{25}-Co (Fig. S80). As illustrated in Fig. 6E, the rate-determining step was the *COOH formation [34,80], with the barrier sequence of TF-COF-CONH-Au_{25}-Co (1.17 eV) < TF-COF-COOH-Co (1.48 eV) < TF-COF-Co (1.76 eV). The lowest energy barrier of TF-COF-CONH-Au_{25}-Co was thermodynamically responsive to its best activity. This sequence cohered with the more negative conduction band from Mott–Schottky analysis for TF-COF-CONH-Au_{25}-Co, which provided a greater thermodynamic driving force for interfacial electron transfer, and with its longest TA carrier lifetime, indicating a larger steady-state electron population reaching the surface [81]. Together, these factors complemented the lowest computed kinetic barrier and rationalize the highest activity. Consistently, hydrogen evolution reaction (HER) energetics (Fig. 6F) revealed

that TF-COF-CONH-Au_{25}-Co has a smaller barrier for *H generation (1.48 eV) than TF-COF-Co (1.61 eV) and TF-COF-COOH-Co (1.97 eV), explaining its superior H_2 evolution rate and syngas productivity.

Differential charge density and Bader charge analyses (Fig. S81) revealed that –COOH functionalization boosted electron transfer from the COF framework to the Co center, increasing from 0.65 e in TF-COF-Co to 0.94 e in TF-COF-COOH-Co [53,82]. Incorporation of Au_{25} NCs further increased electron transfer to 0.98 e, indicating that covalent Au–amide bonding strengthens Co–COF coupling and facilitates interfacial charge transport. Moreover, a near-linear correlation between Co 2p binding energy shifts and Bader charges (Fig. S82) placed TF-COF-CONH-Au_{25}-Co at the largest positive shift/charge depletion, quantitatively evidencing strong Au_{25}-induced electronic modulation at the Co center [22,83]. A mechanistic model is thus proposed in Fig. 6G. Under illumination, photogenerated holes are consumed by the sacrificial agent, while electrons migrate via the amide linkage to the lowest unoccupied molecular orbitals (LUMOs) of Au_{25} NCs, which act as electron reservoirs [74,84]. These electrons are subsequently transferred to the CO_2-adsorbed $[Co(bpy)_3]^{2+}$ site through the COF framework (Fig. 6G), driving CO formation [55]. The synergistic effect of covalent anchoring and interfacial electrostatics not only stabilizes Au_{25} NCs but also optimizes the Co electronic environment, thereby lowering the barrier of the rate-limiting *COOH step and enhancing overall CO_2 reduction efficiency.

Conclusion

Atomically precise Au_{25} NCs were covalently immobilized on a carboxyl-functionalized COF via amide bond formation. Sequential incorporation $[Co(bpy)_3]^{2+}$ fabricated a highly efficient, photosensitizer-free heterogeneous catalyst for photocatalytic CO_2 conversion into syngas under visible-light illumination. The immobilized Au NCs serve a dual function. First, they promote light-harvesting and accelerate charge separation and transfer by serving simultaneously as broadband absorbers and efficient electron sinks. Second, they adjust the electronic structure of nearby Co sites, optimizing intermediates binding and lowering the activation barrier of the rate-limiting step. This work presents a molecularly engineered photocatalyst that integrates $[Co(bpy)_3]^{2+}$, COFs, and atomically precise metal NCs into a unified platform, highlighting the great prospect of COFs as functional supports for metal NCs toward high-performance solar-to-chemical energy conversion.

Materials and Methods

Synthesis of TF-COF

To synthesize TF-COF, a 25-ml Pyrex tube was prepared with TTA (0.17 mmol, 67 mg), TFA (0.17 mmol, 56 mg), *n*-butanol (2.7 ml), *o*-dichlorobenzene (0.9 ml), and 3 M acetic acid (0.45 ml). The mixture was sonicated for 10 min and subsequently degassed at 77 K through 3 freeze–pump–thaw cycles. The tube was then sealed and heated at 120 °C for 3 d. The solid product formed was isolated using centrifugation, followed by successive washing with ethanol (3 × 10 ml) and tetrahydrofuran (THF; 3 × 10 ml). The resultant powder was dried under vacuum, yielding approximately 87% of yellow TF-COF.

Synthesis of TF-COF-COOH

Similarly, a 25-ml Pyrex tube containing TF-COF (63 mg), *n*-butanol (2.7 ml), *o*-dichlorobenzene (0.9 ml), 3 M acetic acid (0.45 ml), *p*-toluenesulfonic acid (TsOH) (20 mg), and pyruvic acid (60 μl) was prepared. The mixture was sonicated for 10 min and degassed at 77 K through 3 freeze–pump–thaw cycles. After sealing, the mixture was heated at 120 °C for 3 d. The solid was collected via centrifugation and subjected to washing with ethanol (3 × 10 ml) and THF (3 × 10 ml). The final product, yellow TF-COF-COOH, was dried under vacuum, yielding an approximate 92% yield.

Synthesis of TF-COF-CONH-Au_{25}

To synthesize TF-COF-CONH-Au_{25}, TF-COF-COOH (40 mg), *N*-hydroxysuccinimide (11.4 mg), and 1-ethyl-3-(3-dimethylaminopropyl)carbodiimide·HCl (37.8 mg) were combined in a 10-ml 2-(*n*-morpholino)ethanesulfonic acid (MES) solution (ethanol/H_2O = 1/5, 4.2 mg·l^{-1}) and stirred for 10 min. Subsequently, a 10-ml solution of Au_{25} NCs (0.57 mg·ml^{-1}) was added to the mixture, which was then stirred for 2 h at room temperature. The resultant solid was isolated via centrifugation, washed with deionized water, and dried under vacuum to obtain the final product.

Preparation of Co-loaded COF TF-COF-CONH-Au_{25}-Co

To prepare the Co-loaded COF, $CoCl_2·6H_2O$ (2 mg, 5.5 μmol) and 2,2′-bipyridine (4.3 mg, 27.5 μmol) were dissolved in 5 ml of MeCN. TF-COF-CONH-Au_{25} (10 mg) was then added to this solution. The mixture was stirred for 12 h under a nitrogen atmosphere at room temperature. Afterward, the solid was isolated through filtration, washed with water, and dried overnight in an oven at 60 °C to yield the Co-loaded product, TF-COF-CONH-Au_{25}-Co. The same method was used for preparing TF-COF-Co and TF-COF-COOH-Co, utilizing the respective COF materials.

Photocatalytic CO_2 reduction

For the photocatalytic CO_2 reduction, a gas-tight quartz reactor (90 ml) was filled with a powder sample (1 mg), MeCN (4 ml), TEOA (1 ml), and a solution of BIH (20 mg). High-purity CO_2 (99.999 vol %) was then bubbled through the reaction mixture for 20 min to completely displace air. A 300-W xenon lamp (Microsolar 300, Beijing Perfectlight Technology Co. Ltd.) equipped with a UV cutoff filter ($\lambda \geq 400$ nm) served as the light source to initiate the reaction at room temperature. The reaction setup was stirred vigorously using a magnetic stirrer throughout the photocatalytic process. After the reaction, gas samples were collected and analyzed using gas chromatography (GC-9860-5CNJ, Nanjing Hope Analytical Equipment Co. Ltd., China), using calibrations with standard gas mixtures. Hydrogen was detected using a thermal conductivity detector, while a flame ionization detector was utilized for measuring carbon monoxide and other hydrocarbons. The liquid phase products underwent identification through ^{1}H NMR analysis. To evaluate the recycling potential of the catalyst, a 4-run recycling test was conducted, where, after each cycle, the catalyst was cleaned with water and subsequently isolated by centrifugation for the next cycle. To investigate the practical applicability, the catalytic efficiency of TF-COF-CONH-Au_{25}-Co was evaluated in an open-air environment on the rooftop of a laboratory building from 2025 October 9 to 12.

XAFS analysis

XAFS spectra were measured at the XAFCA beamline of Singapore Synchrotron Light Source with an electron energy of 0.7 GeV. Athena program was used for the energy calibration, background removal, and Fourier transform of the XAFS spectra. EXAFS fitting was conducted using Artemis software.

Neutron total scattering

Neutron total scattering data were collected on a Multi-Physics Instrument at China Spallation Neutron Source (CSNS), Dongguan, China. The samples were pretreated under vacuum at 393 K for 3 h and then cooled to 10 K for the measurement. The total scattering $S(Q)$ data were converted to PDF $G(r)$ data through Fourier transformation. *d*-PDF spectrum was calculated from the PDF data of the COFs before and after Au_{25} NCs or $[Co(bpy)_3]^{2+}$ loading. PDF refinement was carried out on the program Topas-academic v.7. The structural models involved in the refinements were constructed according to the results of PXRD refinement, structure optimization by DFT calculation, and XANES simulation.

In situ spectral and theoretical study

In situ ATR-SEIRAS spectra were collected on a Thermo Fisher Scientific Nicolet iS50 spectrometer (USA). DFT calculation was performed with the Vienna Ab initio Simulation Package. Experimental procedures for the in situ spectroscopy and computational details, together with other characterizations, are available in the Supplementary Materials.

Acknowledgments

The computational resources provided by the High-Performance Computing Center of Nanjing Tech University are greatly appreciated. We thank the staff members of the Multi-Physics Instrument (https://cstr.cn/31113.02.CSNS.MPI) at the China Spallation Neutron Source (CSNS) (https://cstr.cn/31113.02.CSNS) for providing technical support and assistance in data collection and analysis.

Funding: We are thankful for the funding from the National Natural Science Foundation of China (grants 22222806, 22178162, 22408170, and 22072065), the Distinguished Youth Foundation of Jiangsu Province (BK20220053), National Key Research and Development Program of China (2024YFE0206900), the Six Talent Peaks Project in Jiangsu Province (grant JNHB-035), and the State Key Laboratory of Materials-Oriented Chemical Engineering (nos. SKL-MCE-24A06 and SKL-MCE-25B01).

Author contributions: P.F. carried out most of the experiments, analyzed the data, and wrote the original manuscript. B.M. assisted in the theoretical calculation and analyzed the neutron total scattering data. Q.H. and S.X. performed the XAFS measurement. J. Wei collected the neutron total scattering data. Q.Y., M.S., and Q.X. were involved in the material synthesis and characterization. X.L. and W.Y. participated in the data analysis. Y.Z. and J. Wang supervised the project and revised the manuscript. All authors discussed the results and commented on the manuscript.

Competing interests: The authors declare that they have no competing interests.

Data Availability

All data are available in the manuscript or Supplementary Materials or from the author.

Supplementary Materials

Supplementary Text
Figs. S1 to S82
Tables S1 to S7
References [85–112]

References

1. Fang S, Rahaman M, Bharti J, Reisner E, Robert M, Ozin GA, Hu YH. Photocatalytic CO_2 reduction. *Nat Rev Methods Primers*. 2023;3(1):61.
2. Xue Z-H, Luan D, Zhang H, Lou XW. Single-atom catalysts for photocatalytic energy conversion. *Joule*. 2022;6(1):92–133.
3. Hu Y, Yu C, Wang S, Wang Q, Reinhard M, Zhang G, Zhan F, Wang H, Skoien D, Kroll T, et al. Identifying a highly efficient molecular photocatalytic CO_2 reduction system via descriptor-based high-throughput screening. *Nat Catal*. 2025;8(2):126–136.
4. Liu B, Wang T, Wang S, Zhang G, Zhong D, Yuan T, Dong H, Wu B, Gong J. Back-illuminated photoelectrochemical flow cell for efficient CO_2 reduction. *Nat Commun*. 2022;13(1):7111.
5. Nikoloudakis E, López-Duarte I, Charalambidis G, Ladomenou K, Ince M, Coutsolelos AG. Porphyrins and phthalocyanines as biomimetic tools for photocatalytic H_2 production and CO_2 reduction. *Chem Soc Rev*. 2022;51(16):6965–7045.
6. Lu M, Zhang M, Liu J, Chen Y, Liao JP, Yang MY, Cai YP, Li SL, Lan YQ. Covalent organic framework based functional materials: Important catalysts for efficient CO_2 utilization. *Angew Chem Int Ed Engl*. 2022;61(15):Article e202200003.
7. Kumagai H, Tamaki Y, Ishitani O. Photocatalytic systems for CO_2 reduction: Metal-complex photocatalysts and their hybrids with photofunctional solid materials. *Acc Chem Res*. 2022;55(7):978–990.
8. Mohata S, Majumder P, Banerjee R. Design and structure-function interplay in covalent organic frameworks for photocatalytic CO_2 reduction. *Chem Soc Rev*. 2025;54:6062–6087.
9. Yao Q, Zhu M, Yang Z, Song X, Yuan X, Zhang Z, Hu W, Xie J. Molecule-like synthesis of ligand-protected metal nanoclusters. *Nat Rev Mater*. 2025;10(2):89–108.
10. Li S, Li N-N, Dong X-Y, Zang S-Q, Mak TCW. Chemical flexibility of atomically precise metal clusters. *Chem Rev*. 2024;124(11):7262–7378.
11. Jin R, Zeng C, Zhou M, Chen Y. Atomically precise colloidal metal nanoclusters and nanoparticles: Fundamentals and opportunities. *Chem Rev*. 2016;116(18):10346–10413.
12. Ru HY, Yang JK, Yang YN, Wan QY, Zhu MJ, Hu JH, Li J, Li Q, Zhou M, Li G, et al. Unprecedented stacking-dependent piezoluminescence enhancement in atomically precise superatomic gold nanoclusters. *Sci Adv*. 2025;11(22):eadv0298.
13. Li Y, Zhou M, Jin R. Programmable metal nanoclusters with atomic precision. *Adv Mater*. 2021;33(46):2006591.
14. Yang D, Wang J, Wang Q, Yuan Z, Dai Y, Zhou C, Wan X, Zhang Q, Yang Y. Electrocatalytic CO_2 reduction over atomically precise metal nanoclusters protected by organic ligands. *ACS Nano*. 2022;16(10):15681–15704.
15. Liu Z, Chen J, Li B, Jiang D-E, Wang L, Yao Q, Xie J. Enzyme-inspired ligand engineering of gold nanoclusters for

electrocatalytic microenvironment manipulation. *J Am Chem Soc*. 2024;146(17):11773–11781.
16. Qin Z, Li Z, Sharma S, Peng Y, Jin R, Li G. Self-assembly of silver clusters into one- and two-dimensional structures and highly selective methanol sensing. *Research*. 2022;2022:Article 0018.
17. Wang H, Zhang X, Zhang W, Zhou M, Jiang HL. Heteroatom-doped Ag_{25} nanoclusters encapsulated in metal-organic frameworks for photocatalytic hydrogen production. *Angew Chem Int Ed Engl*. 2024;63(17):Article e202401443.
18. Sun QY, He HZ, Zhou Y, Dai YP, Shang P, Jiang XF. Photocatalytic hydroxylation and oxidative coupling reactions mediated by multinuclear Au(I) supramolecular clusters. *Angew Chem Int Ed Engl*. 2025;64(8):Article e202420499.
19. Kollmannsberger KL, Kronthaler L, Jinschek JR, Fischer RA. Defined metal atom aggregates precisely incorporated into metal-organic frameworks. *Chem Soc Rev*. 2022;51(24): 9933–9959.
20. Yao A, Du Y, Han M, Wang Y, Hu J, Zhu Q, Sheng H, Zhu M. Covalence bridge atomically precise metal nanocluster and metal-organic frameworks for enhanced photostability and photocatalysis. *Nano Res*. 2022;16(1):1527–1532.
21. Huang R-W, Wei Y-S, Dong X-Y, Wu X-H, Du C-X, Zang S-Q, Mak TCW. Hypersensitive dual-function luminescence switching of a silver-chalcogenolate cluster-based metal-organic framework. *Nat Chem*. 2017;9(7):689–697.
22. Wang H, Liu X, Yang W, Mao G, Meng Z, Wu Z, Jiang H-L. Surface-clean Au_{25} nanoclusters in modulated microenvironment enabled by metal-organic frameworks for enhanced catalysis. *J Am Chem Soc*. 2022;144(48): 22008–22017.
23. Cai X, Tian Y, Wang H, Huang S, Liu X, Li G, Ding W, Zhu Y. Catalytic N-formylation of CO_2 by atomically precise $Au_8Pd_1(DPPF)_4^{2+}$ clusters into a two-dimensional metal-organic framework. *Angew Chem Int Ed Engl*. 2024;64(1):Article e202414030.
24. Wang X, Zhao J, Eliasson H, Erni R, Ziarati A, McKeown Walker S, Bürgi T. Very low temperature CO oxidation over atomically precise Au_{25} nanoclusters on MnO_2. *J Am Chem Soc*. 2023;145(50):27273–27281.
25. Ma T, Kapustin EA, Yin SX, Liang L, Zhou Z, Niu J, Li LH, Wang Y, Su J, Li J, et al. Single-crystal x-ray diffraction structures of covalent organic frameworks. *Science*. 2018;361(6397):48–52.
26. Guan Q, Zhou LL, Dong YB. Metalated covalent organic frameworks: From synthetic strategies to diverse applications. *Chem Soc Rev*. 2022;51(15):6307–6416.
27. Liu R, Chen Y, Yu H, Položij M, Guo Y, Sum TC, Heine T, Jiang D. Linkage-engineered donor-acceptor covalent organic frameworks for optimal photosynthesis of hydrogen peroxide from water and air. *Nat Catal*. 2024;7(2):195–206.
28. Huang Y, Du P, Shi WX, Wang Y, Yao S, Zhang ZM, Lu TB, Lu X. Filling COFs with bimetallic nanoclusters for CO_2-to-alcohols conversion with H_2O oxidation. *Appl Catal B*. 2021;288:Article 120001.
29. Zou L, Chen ZA, Si DH, Yang SL, Gao WQ, Wang K, Huang YB, Cao R. Boosting CO_2 photoreduction via regulating charge transfer ability in a one-dimensional covalent organic framework. *Angew Chem Int Ed Engl*. 2023;62(46):Article e202309820.
30. Chen H, Jena HS, Feng X, Leus K, Van Der Voort P. Engineering covalent organic frameworks as heterogeneous photocatalysts for organic transformations. *Angew Chem Int Ed Engl*. 2022;61(47):Article e202204938.
31. Chen L, Chen G, Gong C, Zhang Y, Xing Z, Li J, Xu G, Li G, Peng Y. Low-valence platinum single atoms in sulfur-containing covalent organic frameworks for photocatalytic hydrogen evolution. *Nat Commun*. 2024;15(1):10501.
32. Fu P, Chen C, Wu C, Meng B, Yue Q, Chen T, Yin W, Chi X, Yu X, Li R, et al. Covalent organic framework stabilized single CoN_4Cl_2 site boosts photocatalytic CO_2 reduction into tunable syngas. *Angew Chem Int Ed Engl*. 2025;64(3): Article e202415202.
33. Teng ZY, Zhang ZZ, Yang HB, Zhang QT, Ohno T, Su CL. Atomically isolated $Sb(CN)_3$ on sp^2-c-COFs with balanced hydrophilic and oleophilic sites for photocatalytic C-H activation. *Sci Adv*. 2024;10(5):eadl5432.
34. Ran L, Li Z, Ran B, Cao J, Zhao Y, Shao T, Song Y, Leung MK, Sun L, Hou J. Engineering single-atom active sites on covalent organic frameworks for boosting CO_2 Photoreduction. *J Am Chem Soc*. 2022;144(37):17097–17109.
35. Das P, Chakraborty G, Roeser J, Vogl S, Rabeah J, Thomas A. Integrating Bifunctionality and chemical stability in covalent organic frameworks via one-pot multicomponent reactions for solar-driven H_2O_2 production. *J Am Chem Soc*. 2023;145(5):2975–2984.
36. Yang Y, Yu L, Chu T, Niu H, Wang J, Cai Y. Constructing chemical stable 4-carboxyl-quinoline linked covalent organic frameworks via Doebner reaction for nanofiltration. *Nat Commun*. 2022;13(1):2615.
37. Lyu W, Liu Y, Chen D, Wang F, Li Y. Engineering the electron localization of metal sites on nanosheets assembled periodic macropores for CO_2 photoreduction. *Nat Commun*. 2024;15(1):10589.
38. Hwang GB, Huang H, Wu G, Shin J, Kafizas A, Karu K, Toit HD, Alotaibi AM, Mohammad-Hadi L, Allan E, et al. Photobactericidal activity activated by thiolated gold nanoclusters at low flux levels of white light. *Nat Commun*. 2020;11(1):1207.
39. Xie Y, Pan T, Lei Q, Chen C, Dong X, Yuan Y, Maksoud WA, Zhao L, Cavallo L, Pinnau I, et al. Efficient and simultaneous capture of iodine and methyl iodide achieved by a covalent organic framework. *Nat Commun*. 2022;13(1):2878.
40. Lu M, Zhang M, Liu J, Yu TY, Chang JN, Shang LJ, Li SL, Lan YQ. Confining and highly dispersing single polyoxometalate clusters in covalent organic frameworks by covalent linkages for CO_2 photoreduction. *J Am Chem Soc*. 2022;144(4):1861–1871.
41. Zhou J, Li J, Kan L, Zhang L, Huang Q, Yan Y, Chen Y, Liu J, Li SL, Lan YQ. Linking oxidative and reductive clusters to prepare crystalline porous catalysts for photocatalytic CO_2 reduction with H_2O. *Nat Commun*. 2022;13(1):4681.
42. Cui X, Wang J, Liu B, Ling S, Long R, Xiong Y. Turning Au nanoclusters catalytically active for visible-light-driven CO_2 reduction through bridging ligands. *J Am Chem Soc*. 2018;140(48):16514–16520.
43. Zhuo S, Wang X, Li L, Yang S, Ji Y. Chiral carboxyl-functionalized covalent organic framework for enantioselective adsorption of amino acids. *ACS Appl Mater Interfaces*. 2021;13(26):31059–31065.
44. Li G, Yue Q, Fu P, Wang K, Zhou Y, Wang J. Ionic dye based covalent organic frameworks for photothermal water evaporation. *Adv Funct Mater*. 2023;33(34):2213810.
45. Phongamwong T, Barrabés N, Donphai W, Witoon T, Rupprechter G, Chareonpanich M. Chlorophyll-modified

$Au_{25}(SR)_{18}$-functionalized TiO_2 for photocatalytic degradation of rhodamine B. *Appl Catal B*. 2023;325:Article 122336.
46. Chen C, Ye C, Zhao X, Zhang Y, Li R, Zhang Q, Zhang H, Wu Y. Supported Au single atoms and nanoparticles on MoS_2 for highly selective CO_2-to-CH_3COOH photoreduction. *Nat Commun*. 2024;15(1):7825.
47. Yu J, Gao RT, Guo X, Truong Nguyen N, Wu L, Wang L. Electrochemical nitrate reduction to ammonia on AuCu single-atom alloy aerogels under wide potential window. *Angew Chem Int Ed Engl*. 2025;64(4):Article e202415975.
48. Shivhare A, Lee KE, Hu Y, Scott RWJ. Following the reactivity of $Au_{25}(SC_8H_9)_{18}^-$ clusters with Pd^{2+} and Ag^+ ions using in situ x-ray absorption spectroscopy: A tale of two metals. *J Phys Chem C*. 2015;119(40):23279–23284.
49. Wang H, Liu X, Zhao Y, Sun Z, Lin Y, Yao T, Jiang H-L. Regulating interaction with surface ligands on Au_{25} nanoclusters by multivariate metal-organic framework hosts for boosting catalysis. *Natl Sci Rev*. 2024;11(10):Article nwae252.
50. Romero-Muñiz I, Mavrandonakis A, Albacete P, Vega A, Briois V, Zamora F, Platero-Prats AE. Unveiling the local structure of palladium loaded into imine-linked layered covalent organic frameworks for cross-coupling catalysis. *Angew Chem Int Ed Engl*. 2020;59(31):13013–13020.
51. He Y, Zhao Y, Wang X, Liu Z, Yu Y, Li L. Multiple heteroatom-hydrogen bonds bridging electron transport in covalent organic framework-based supramolecular system for photoreduction of CO_2. *Angew Chem Int Ed Engl*. 2023;62(31):Article e202307160.
52. Zhou M, Wang Z, Mei A, Yang Z, Chen W, Ou S, Wang S, Chen K, Reiss P, Qi K, et al. Photocatalytic CO_2 reduction using La-Ni bimetallic sites within a covalent organic framework. *Nat Commun*. 2023;14(1):2473.
53. Deng A, Zhao E, Li Q, Sun Y, Liu Y, Yang S, He H, Xu Y, Zhao W, Song H, et al. Atomic cobalt-silver dual-metal sites confined on carbon nitride with synergistic Ag nanoparticles for enhanced CO_2 photoreduction. *ACS Nano*. 2023;17(12):11869–11881.
54. Zhou L, Qu Z, Fu L, Ding Y. Interfacial engineering of In-SnO_2 heterostructure for promoting electrocatalytic CO_2 reduction to formate. *Appl Catal B*. 2025;377:Article 125471.
55. Yu M, Chen W, Lin Q, Li L, Liu Z, Bi J, Yu Y. Electrostatic confinement-induced excited charge transfer in ionic covalent organic framework promoting CO_2 reduction. *Angew Chem Int Ed Engl*. 2025;64(6):Article e202418422.
56. Zeng R, Sun C, Lin Z, Li Y, Zhou C, Zhang S, Li L, Guo S. Biomimetic interface with dynamic disulfide bonds boosts durable photoconversion of diluted CO_2. *J Am Chem Soc*. 2025;147(42):38311–38319.
57. Li M, Zuo Z, Zhang S. High-density ultrafine Au nanocluster-doped Co-LDH nanocages for enhanced visible-light-driven CO_2 reduction. *ACS Catal*. 2023;13(17):11815–11824.
58. Tian J, Zhong K, Zhu X, Yang J, Mo Z, Liu J, Dai J, She Y, Song Y, Li H, et al. Highly exposed active sites of Au nanoclusters for photocatalytic CO_2 reduction. *Chem Eng J*. 2023;451:Article 138392.
59. Xiang Y, Dong W, Wang P, Wang S, Ding X, Ichihara F, Wang Z, Wada Y, Jin S, Weng Y, et al. Constructing electron delocalization channels in covalent organic frameworks powering CO_2 photoreduction in water. *Appl Catal B*. 2020;274:Article 119096.
60. Liang J, Zhang H, Song Q, Liu Z, Xia J, Yan B, Meng X, Jiang Z, Lou XW, Lee CS. Modulating charge separation of oxygen-doped boron nitride with isolated Co atoms for enhancing CO_2-to-CO photoreduction. *Adv Mater*. 2024;36(1):2303287.
61. Yang S, Hu W, Zhang X, He P, Pattengale B, Liu C, Cendejas M, Hermans I, Zhang X, Zhang J, et al. 2D covalent organic frameworks as intrinsic photocatalysts for visible light-driven CO_2 reduction. *J Am Chem Soc*. 2018;140(44):14614–14618.
62. Lin H, Liu Y, Wang Z, Ling L, Huang H, Li Q, Cheng L, Li Y, Zhou J, Wu K, et al. Enhanced CO_2 photoreduction through spontaneous charge separation in end-capping assembly of heterostructured covalent-organic frameworks. *Angew Chem Int Ed Engl*. 2022;61(50):Article e202214142.
63. Lei B, Zhou G, Gong Z, Liu C, Zhou Y, Guro VP, Sun Y, Sheng J, Dong F. Dynamically cyclic Fe^{2+}/Fe^{3+} active sites as electron and proton-feeding centers boosting CO_2 photoreduction powered by benzyl alcohol oxidation. *Research*. 2024;8:Article 0567.
64. Yang Y, Zhang HY, Wang Y, Shao LH, Fang L, Dong H, Lu M, Dong LZ, Lan YQ, Zhang FM. Integrating enrichment, reduction, and oxidation sites in one system for artificial photosynthetic diluted CO_2 reduction. *Adv Mater*. 2023;35(40):2304170.
65. Yue Q, Zhang Z, Liu X, Zhu C, Wen Y, Fu P, Hu Q, Qu X, Zhou Y, Wang J. Engineering electron delocalization of ultrathin covalent organic framework nanosheets to elevate photocatalytic hydrogen evolution in seawater. *Chem Eng J*. 2025;507:Article 160481.
66. Chen Q, Liu Y, Gu X, Li D, Zhang D, Zhang D, Huang H, Mao B, Kang Z, Shi W. Carbon dots mediated charge sinking effect for boosting hydrogen evolution in Cu-In-Zn-S QDs/MoS_2 photocatalysts. *Appl Catal B*. 2022;301:Article 120755.
67. Zhang LX, Qi MY, Tang ZR, Xu YJ. Heterostructure-engineered semiconductor quantum dots toward photocatalyzed-redox cooperative coupling reaction. *Research*. 2023;6:Article 0073.
68. Liu Y, Sun J, Huang H, Bai L, Zhao X, Qu B, Xiong L, Bai F, Tang J, Jing L. Improving CO_2 photoconversion with ionic liquid and Co single atoms. *Nat Commun*. 2023;14(1):1457.
69. Yang S, Byun WJ, Zhao F, Chen D, Mao J, Zhang W, Peng J, Liu C, Pan Y, Hu J, et al. CO_2 enrichment boosts highly selective infrared-light-driven CO_2 conversion to CH_4 by UiO-66/Co_9S_8 photocatalyst. *Adv Mater*. 2024;36(16):2312616.
70. Cheng K, Kong S, Wang J, Wang Q, Yuan S, Li PZ, Zhao Y. Integrating multifunctionalities into a 3D covalent organic framework for efficient CO_2 photoreduction. *Angew Chem Int Ed Engl*. 2025;64(26):Article e202504772.
71. Cao Y, Yu W, Li Y, Meng J, Zheng K, Huang C, Yang X, Yang Y, Dong F, Zhou Y. Engineering ultrafast photo-induced charge and carbon intermediates transfer at Interface to break the activity-selectivity trade-off in direct conversion of methane to methanol. *Adv Energy Mater*. 2024;15(6):2404871.
72. Qiu J, Meng K, Zhang Y, Cheng B, Zhang J, Wang L, Yu J. COF/In_2S_3 S-scheme Photocatalyst with enhanced light absorption and H_2O_2-production activity and fs-TA investigation. *Adv Mater*. 2024;36(24):2400288.
73. Yu Y, Dong XA, Chen P, Geng Q, Wang H, Li J, Zhou Y, Dong F. Synergistic effect of Cu single atoms and Au-Cu alloy nanoparticles on TiO_2 for efficient CO_2 photoreduction. *ACS Nano*. 2021;15(9):14453–14464.

74. Yan X, Fu XY, Xiao FX. Filling the gap: Atomically precise metal nanoclusters-induced Z-scheme photosystem toward robust and stable solar hydrogen generation. *Adv Funct Mater*. 2023;33(48):2303737.
75. Chen X, Dang Q, Sa R, Li L, Li L, Bi J, Zhang Z, Long J, Yu Y, Zou Z. Integrating single Ni sites into biomimetic networks of covalent organic frameworks for selective photoreduction of CO_2. *Chem Sci*. 2020;11(26):6915–6922.
76. Wang J, Xia T, Wang L, Zheng X, Qi Z, Gao C, Zhu J, Li Z, Xu H, Xiong Y. Enabling visible-light-driven selective CO_2 reduction by doping quantum dots: Trapping electrons and suppressing H_2 evolution. *Angew Chem Int Ed Engl*. 2018;57(50):16447–16451.
77. Zhang AA, Wang ZX, Fang ZB, Li JL, Liu TF. Long-range π-π stacking brings high electron delocalization for enhanced photocatalytic activity in hydrogen-bonded organic framework. *Angew Chem Int Ed Engl*. 2024;63(46): Article e202412777.
78. Wang J, Zhu W, Meng F, Bai G, Zhang Q, Lan X. Integrating dual-metal sites into covalent organic frameworks for enhanced photocatalytic CO_2 reduction. *ACS Catal*. 2023;13(7):4316–4329.
79. Su B, Wang S, Xing W, Liu K, Hung SF, Chen X, Fang Y, Zhang G, Zhang H, Wang X. Synergistic Ru species on poly(heptazine imide) enabling efficient photocatalytic CO_2 reduction with H_2O beyond 800 nm. *Angew Chem Int Ed Engl*. 2025;64(27):Article e202505453.
80. Liu Z, Yin H, Sun J, Bai L, Li Z, Zhao X, Yan X, Zhao M, Jing L. Engineering single Cu atoms anchored via N-heterocyclic carbene in COF mesopores for modulating electron kinetics of CO_2 photoconversion. *Adv Energy Mater*. 2024;14(33):2401713.
81. Gu X, Niu H, Shi Y, Ding H, Cai Y, Jiang G. Cross-shaped donor-π-acceptor covalent organic frameworks with tunable push-pull architectures for effective photocatalytic H_2O_2 production. *Angew Chem Int Ed Engl*. 2025;65(5): Article e20491.
82. Yu Y, He Y, Yan P, Wang S, Dong F. Boosted C-C coupling with Cu-Ag alloy sub-nanoclusters for CO_2-to-C_2H_4 photosynthesis. *Proc Natl Acad Sci USA*. 2023;120(44): Article e2307320120.
83. Li T, Yang Z, Xu Q, Sun T, Ma X, Zheng T, Wang Y, Wang Z, Li Q, Yu Q, et al. Asymmetrical degree engineered carbon dioxide photoreduction for single atomic Co sites on polymeric carbon nitride. *Adv Funct Mater*. 2025;35(51): Article e11356.
84. Ziarati A, Zhao J, Afshani J, Kazan R, Perez Mellor A, Rosspeintner A, McKeown S, Bürgi T. Advanced catalyst for CO_2 photo-reduction: From controllable product selectivity by architecture engineering to improving charge transfer using stabilized Au clusters. *Small*. 2023;19(24):Article 2207857.
85. Tan Y, Yan L, Huang C, Zhang W, Qi H, Kang L, Pan X, Zhong Y, Hu Y, Ding Y. Fabrication of an Au_{25}-Cys-Mo electrocatalyst for efficient nitrogen reduction to ammonia under ambient conditions. *Small*. 2021;17(21):2100372.
86. Wang C, Lv P, Xue D, Cai Y, Yan X, Xu L, Fang J, Yang Y. Zero-dimensional/two-dimensional $Au_{25}(Cys)_{18}$ nanoclusters/g-C_3N_4 nanosheets composites for enhanced photocatalytic hydrogen production under visible light. *ACS Sustain Chem Eng*. 2018;6(7):8447–8457.
87. Lam E, Reisner E. A TiO_2-Co(terpyridine)$_2$ photocatalyst for the selective oxidation of cellulose to formate coupled to the reduction of CO_2 to syngas. *Angew Chem Int Ed Engl*. 2021;60(43):23306–23312.
88. Bonchio M, Bonin J, Ishitani O, Lu TB, Morikawa T, Morris AJ, Reisner E, Sarkar D, Toma FM, Robert M. Best practices for experiments and reporting in photocatalytic CO_2 reduction. *Nat Catal*. 2023;6(8):657–665.
89. Kudo A, Miseki Y. Heterogeneous photocatalyst materials for water splitting. *Chem Soc Rev*. 2009;38(1):253–278.
90. Qureshi M, Takanabe K. Insights on measuring and reporting heterogeneous photocatalysis: Efficiency definitions and setup examples. *Chem Mater*. 2016;29(1):158–167.
91. Kresse G, Furthmüller J. Efficient iterative schemes for ab initio total-energy calculations using a plane-wave basis set. *Phys Rev B*. 1996;54(16):11169.
92. Kresse G, Furthmüller J. Efficiency of ab-initio total energy calculations for metals and semiconductors using a plane-wave basis set. *Comput Mater Sci*. 1996;6(1):15–50.
93. Perdew JP, Burke K, Ernzerhof M. Generalized gradient approximation made simple. *Phys Rev Lett*. 1996;77(18):3865–3868.
94. Kresse G, Joubert D. From ultrasoft pseudopotentials to the projector augmented-wave method. *Phys Rev B*. 1999;59(3):1758.
95. Blöchl PE. Projector augmented-wave method. *Phys Rev B*. 1994;50(24):17953.
96. Bhati M, Chen Y, Senftle TP. Density functional theory modeling of photo-electrochemical reactions on semiconductors: H_2 evolution on 3C-SiC. *J Phys Chem C*. 2020;124(49):26625–26639.
97. Gauthier JA, Ringe S, Dickens CF, Garza AJ, Bell AT, Head-Gordon M, Nørskov JK, Chan K. Challenges in modeling electrochemical reaction energetics with polarizable continuum models. *ACS Catal*. 2019;9(2):920–931.
98. Mathew K, Sundararaman R, Letchworth-Weaver K, Arias TA, Hennig RG. Implicit solvation model for density-functional study of nanocrystal surfaces and reaction pathways. *J Chem Phys*. 2014;140(8):Article 084106.
99. Heaven MW, Dass A, White PS, Holt KM, Murray RW. Crystal structure of the gold nanoparticle $[N(C_8H_{17})_4][Au_{25}(SCH_2CH_2Ph)_{18}]$. *J Am Chem Soc*. 2008;130(12):3754–3755.
100. Dainese T, Antonello S, Gascon JA, Pan F, Perera NV, Ruzzi M, Venzo A, Zoleo A, Rissanen K, Maran F. $Au_{25}(SEt)_{18}$, a nearly naked thiolate-protected Au_{25} cluster: Structural analysis by single crystal x-ray crystallography and electron nuclear double resonance. *ACS Nano*. 2014;8(4):3904–3912.
101. Xia YS, Tang M, Zhang L, Liu J, Jiang C, Gao GK, Dong LZ, Xie LG, Lan YQ. Tandem utilization of CO_2 photoreduction products for the carbonylation of aryl iodides. *Nat Commun*. 2022;13(1):2964.
102. Tu W, Yang Y, Chen C, Zhou T, Li T, Wang H, Wu S, Zhou Y, O'Hare D, Zou Z, et al. Cu-O/N single sites incorporated 2D covalent organic framework ultrathin nanobelts for highly selective visible-light-driven CO_2 reduction to CO. *Small Struct*. 2022;4(6):2200233.
103. Dong P, Xu X, Luo R, Yuan S, Zhou J, Lei J. Postsynthetic annulation of three-dimensional covalent organic frameworks for boosting CO_2 photoreduction. *J Am Chem Soc*. 2023;145(28):15473–15481.
104. Gong LJ, Liu LY, Zhao SS, Yang SL, Si DH, Wu QJ, Wu Q, Huang YB, Cao R. Rapid charge transfer in covalent organic framework via through-bond for enhanced photocatalytic CO_2 reduction. *Chem Eng J*. 2023;458:Article 141360.

105. Zou L, Sa R, Zhong H, Lv H, Wang X, Wang R. Photoelectron transfer mediated by the interfacial electron effects for boosting visible-light-driven CO_2 reduction. *ACS Catal*. 2022;12(6):3550–3557.
106. Han WK, Li J, Zhu RM, Wei M, Xia SK, Fu JX, Zhang J, Pang H, Li MD, Gu ZG. Photosensitizing metal covalent organic framework with fast charge transfer dynamics for efficient CO_2 photoreduction. *Chem Sci*. 2024;15(22):8422–8429.
107. Qin L, Sun D, Ma D, Wang Z, Liu Y, Li Q, Song F, Wu K, Gan L, Zhou T, et al. Decoupling interlayer interactions boosts charge separation in covalent organic frameworks for high-efficiency photocatalytic CO_2 reduction. *Adv Mater*. 2025;37(29):2504205.
108. Dong H, Fang L, Chen KX, Wei JX, Li JX, Qiao X, Wang Y, Zhang FM, Lan YQ. Dual metallosalen-based covalent organic frameworks for artificial photosynthetic diluted CO_2 reduction. *Angew Chem Int Ed Engl*. 2025;64(2): Article e202414287.
109. He J, Wang X, Jin S, Liu Z-Q, Zhu M. 2D metal-free heterostructure of covalent triazine framework/g-C_3N_4 for enhanced photocatalytic CO_2 reduction with high selectivity. *Chin J Catal*. 2022;43(5):1306–1315.
110. Wang J, Yu Y, Cui J, Li X, Zhang Y, Wang C, Yu X, Ye J. Defective g-C_3N_4/covalent organic framework van der Waals heterojunction toward highly efficient S-scheme CO_2 photoreduction. *Appl Catal B*. 2022;301:Article 120814.
111. Fu Z, Shu C, Wang X, Chen L, Wang X, Liu L, Wang K, Clowes R, Chong SY, Wu X, et al. Fluorinated covalent organic frameworks coupled with molecular cobalt cocatalysts for efficient photocatalytic CO_2 reduction. *CCS Chem*. 2023;5(10):2290–2300.
112. Kim YH, Jeon JP, Kim Y, Noh HJ, Seo JM, Kim J, Lee G, Baek JB. Cobalt-porphyrin-based covalent organic frameworks with donor-acceptor units as photocatalysts for carbon dioxide reduction. *Angew Chem Int Ed Engl*. 2023;62(36):Article e202307991.